# Structural rationale for boson peak in metallic glass informed by an interpretable neural network model

Jia-Le Tao, Zeng-Yu Yang, and Yun-Jiang Wang*

*State Key Laboratory of Nonlinear Mechanics, Institute of Mechanics, Chinese Academy of Sciences, Beijing 100190, China and School of Engineering Science, University of Chinese Academy of Sciences, Beijing 100049, China*

(Received 3 November 2022; accepted 5 May 2023; published 22 May 2023)

In amorphous solids, there exists a universal phenomenon of vibrational anomaly, i.e., an excess of vibrational modes over the Debye level in the low-terahertz-frequency regime, which is termed a *boson peak*. Although the origin of the boson peak has been studied extensively for decades, quantitative prediction of its intensity remains elusive. In this paper, we try to quantify the intensity of the boson peak via an interpretable machine-learning strategy based on a dataset consisting of >1600 glass samples prepared with cooling rates spanning four orders of magnitude. We have attempted to extract information from a pure static structure and vibrational localization through four different feature inputs, among which the partial pair distribution function (PDF) yields the best predictive performance. It is found that the first several neighbor shells corresponding to a characteristic subnanometer length scale are important for capturing the structural genes of the boson peak in amorphous solids, regardless of the size of the glasses. Moreover, a higher boson peak relates to a more disordered atomic arrangement with lower peaks and shallower basins in the PDF. The obtained knowledge sheds light on rationalization of the boson peak in amorphous solids from pure structural information.

DOI: 10.1103/PhysRevResearch.5.023113

## I. INTRODUCTION

The thermal properties of disordered materials such as vitreous $SiO_2$, polymer glasses, confined water solid, amorphous alloys, and strain glass usually present a hump of reduced specific heat $C(T)/T^3$ and a plateau in the temperature dependence of thermal conductivity $\kappa(T)$ at low temperatures [1–6], which are strikingly different from those of the crystalline solids. Such anomalous properties are believed to be controlled by the vibrational spectra in the corresponding low-terahertz-frequency regime, where amorphous solids exhibit an excess of the vibrational density of states (VDOS) over the Debye model (a peak in the $\omega^2$-reduced density of states $g(\omega)/\omega^2$), the so-called *boson peak* [7]. Of great concern has been the origin of the boson peak since its discovery. Though tremendous efforts have been devoted to this controversial but fascinating phenomenon, its nature is still far from fully understood.

Various models have been proposed to interpret this vibrational anomaly. Some ascribe it to structural disorder; others believe that it is an extension of the well-known phenomenon in crystals—the van Hove singularity appearing in the phonon dispersion relationship. These interpretations include the so-called quasilocalized acoustic transverse vibrational modes [8,9] originating from soft anharmonic potentials [10–12], elastic heterogeneity [13–18], local breaking of inversion symmetry [19,20], phonon-saddle transition in the energy landscape [21], the orientational order parameter [22], and broadened van Hove singularity shifted to lower frequencies [23–25]. Despite all this progress, determining a microstructural feature that governs the boson peak due to the complex and disordered atomic arrangement in glasses remains elusive, let alone quantitatively predicting it from pure structural information.

Under this circumstance, data-intensive scientific discovery, known as the fourth paradigm, provides a research framework alternative to the physics-based methodologies [26–29]. For glass science, it has been applied to develop accurate interatomic potentials [30], accelerate the design of glasses [31,32], and construct structure-property relationships [33–41] (e.g., plasticity, relaxation, stiffness), playing a growing important role in the field of amorphous materials.

Inspired by these advancements, in this paper, we refrain from debating the origin of the boson peak but try to resolve the quantitative prediction of it from a data-driven perspective, within either the configurational or dynamic space. Specifically, we select a prototypical binary metallic glass (MG) $Cu_{50}Zr_{50}$ as our research object and generate 1629 glass samples through molecular dynamics (MD) simulations to construct the dataset requisite for machine learning (ML). In this protocol, the total and partial pair distribution functions (PDFs) of the glass samples with different cutoff radius are calculated to depict the local static structure. After diagonalizing the Hessian matrix of the inherent structures, the vibrational spectra, the participation ratio of each normal mode, and the intensity of the boson peak are computed

*yjwang@imech.ac.cn

subsequently. Finally, we turn to the artificial neural network model for regressive predictions and find that the partial PDF yields the best results of all four kinds of feature inputs. Indeed, we roughly succeed in quantifying the intensity of boson peak with the mean absolute error (MAE) equivalent to $7.98\,\mu\mathrm{THz}^{-3}$. It is demonstrated that the first three or four neighbor shells together with specific atom distributions are of vital importance in rationalizing the boson peak, implying a characteristic length scale, also validated at atomic level, that needs to be considered when uncovering the structural nature of properties in amorphous solids.

## II. METHODS

### A. MD

Altogether, 1800 binary $Cu_{50}Zr_{50}$ MG samples with different cooling rates spanning four orders of magnitude are prepared through classical MD simulations, implemented by the open-source LAMMPS code [42]. Each sample contains 4000 atoms with periodic boundary conditions applied in all three directions. An optimized Finnis-Sinclair-type embedded-atom-method potential is utilized to describe the interatomic interaction [43]. The integration time step of MD is set to 2 fs. Under the NPT ensemble, a Nosé-Hoover thermostat [44,45] is used to control the temperature, and the external pressure in each direction is maintained at zero with the Parrinello-Rahman barostat method [46]. The model preparation process can be divided into four steps: heating, relaxation, quenching, and energy minimization from liquid to glassy solid. Each model with randomly distributed atoms in the face-centered cubic (fcc) lattice is first heated from 0 to 2000 K and maintained for 2 ns to ensure it is thermodynamically equilibrated. Then the melt is quenched to 0.1 K with desired cooling rates ranging from $10^{10}$ to $10^{14}$ K/s. Finally, energy minimization with a conjugate gradient algorithm is performed to fully relax the system and obtain an inherent configuration of the glass-forming liquid corresponding to a local energy minimum in the potential energy landscape. To regress the single-atom boson peak intensity, 10 extra larger $Cu_{50}Zr_{50}$ glass samples each containing 19 652 atoms are also simulated with cooling rate $10^{10}$ K/s, among which nine samples are used for training and the remaining one for testing. In this case, the training set contains 176 868 data points and the testing set 19 652.

### B. Feature input

A typical ML process includes several systematical steps, such as data collection, feature extraction, model training and validation, and model evaluation. For a supervised learning task, the completeness of the feature and the quality of the supervisory signal cooperatively determine the predictive performance of the specific ML model as well as the model itself.

#### *1. Partial PDF as feature input*

For amorphous solids lacking long-range order, characterization of its structure has long been challenging. Here, to depict the local configuration of a glass, the simplest PDF is employed. The partial PDF is defined as

$$g_{\alpha\beta}(r) = \frac{1}{N_\alpha \rho_\beta 4\pi r^2 \Delta r} \sum_{i=1}^{N_\alpha} \sum_{j=1}^{N_\beta} \delta(r - r_{ij}), \tag{1}$$

where $\rho_\beta$ and $N_\alpha$ represent the number density and number of atoms of the corresponding species in the subscripts. For the continuity of $g_{\alpha\beta}$ calculated at intervals of $\Delta r = 0.1$Å, we leave this descriptor as it is without feature selection.

As for the atomic structural descriptor, Gaussian-type approximation [47] is adopted to guarantee a smooth and continuous particle-level partial PDF:

$$g^i_{\alpha\beta}(r) = \frac{1}{\rho_\beta 4\pi r^2 \Delta r} \sum_{j=1, r_{ij} \leqslant r_c}^{N_\beta} \exp\left[-(r - r_{ij})^2/\sigma^2\right] \tag{2}$$

that exhibits better performance than the original scattered one. Here, $r_{ij}$ is the distance between atoms $i$ and $j$, $r_c$ is the cutoff radius, and $\sigma$ is a broadening coefficient.

#### *2. Participation ratio as feature input*

There are reports of another kind of quasilocalized excess mode at frequencies lower than the boson peak frequency, whose density of states obeys a quartic law with respect to frequency [48–53]. To some extent, this phenomenon is believed to be connected to the boson peak [49,53,54], though it does not affect its intensity mathematically. Thus, we try to construct a connection between them by quantifying the boson peak from the perspective of vibrational localization in the present ML model. Following the common practice [49,52], the participation ratio is utilized to divide normal modes into two categories: quasilocalized and extended. The participation ratio of the normal mode $l$ is defined as

$$P(\omega_l) = \frac{\left(\sum_{i=1}^{N} \left|\mathbf{e}_l^i\right|^2\right)^2}{N \sum_{i=1}^{N} \left|\mathbf{e}_l^i\right|^4}, \tag{3}$$

where $N$ and $\mathbf{e}_l^i$ denote the total number of atoms and the polarization vector of atom $i$ under the eigenfrequency $\omega_l$. Of all the normal modes sorted by the vibrational frequency with ascending order, the first 724 modes within the boson peak frequency region are selected ($\omega \leqslant 10$ THz), the participation ratios $P(\omega)$ of which are then used as the feature input, i.e., a 724-dimensional vector $\mathbf{P} = \{P_1, P_2, \ldots, P_{724}\}^\top$. We also tried a modified version of $\mathbf{P}$. Based on some threshold $P_0$, $\mathbf{P}$ is binarized: if $P_i < P_0$, $P_i \leftarrow 1$; else $P_i \leftarrow 0$. Thresholds between 0.02 and 0.42 with intervals of 0.02 are tested, and the best results are obtained when $P_0$ lies between 0.24 and 0.30 (see Appendix A).

### C. Supervisory signal

Normal mode analysis is implemented by directly diagonalizing the dynamic matrix of the inherent structure to obtain the VDOS, as shown in Fig. 1(a). The intensity of the boson peak is characterized by the maximum of $\omega^2$-reduced VDOS $g(\omega)/\omega^2$, which serves as the supervisory signal. The sampling interval of the power exponent of the cooling rate is first uniformly set to 0.005 from $10^{10}$ to $10^{14}$ K/s. As illustrated in Fig. 1(b), the intensity of boson peak $I_{\mathrm{BP}}$ enhances, and

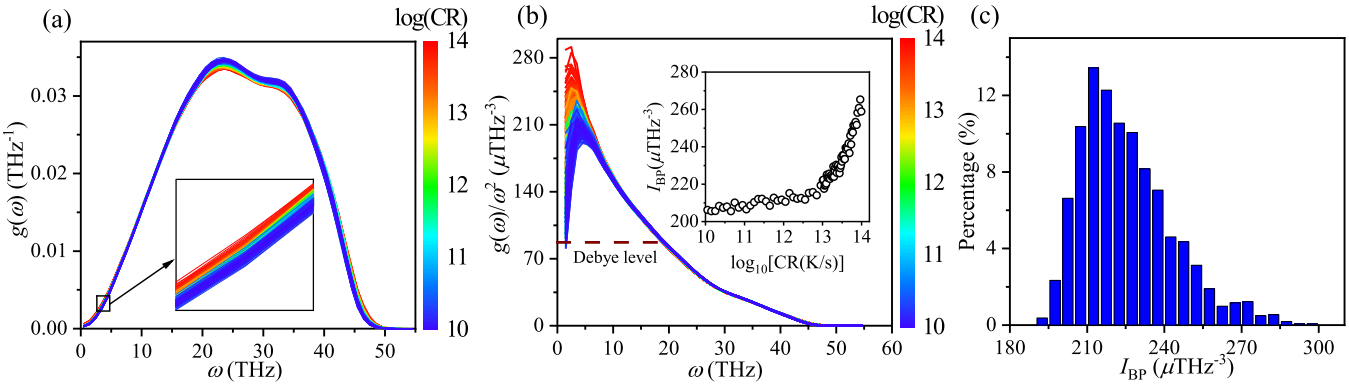


FIG. 1. Relevance between cooling rate and the intensity of boson peak. (a) Vibrational density of states (VDOS) of the glass samples with different cooling rates ranging from $10^{10}$ to $10^{14}$ K/s. The inset shows that higher cooling rate leads to increasing soft modes, corresponding to higher boson peak intensity in (b). (b) $\omega^2$-reduced VDOS in (a). The dashed line indicates the Debye level. The inset illustrates that the boson peak intensity enhances when cooling rate increases. (c) Distribution of the boson peak intensity.

the corresponding frequency $\omega_{BP}$ shifts to lower frequencies with the increase of the cooling rate, but this relation levels off gently when the cooling rate is $<10^{13}$ K/s. To acquire a well-distributed $I_{BP}$, detailed data points between $10^{13}$ and $10^{14}$ K/s with interval 0.001 K/s are supplemented; thus, a total of 1800 model glasses are prepared. When the cooling rate is $>10^{13}$ K/s, the $g(\omega)/\omega^2 - \omega$ curve of some glass samples shows a monotonic decreasing about $\omega$; thus, the boson peak intensities of these samples defined by $\max[g(\omega)/\omega^2]$ become unreliable. After eliminating such irrational data, a final dataset with 1629 MG samples is constructed [see Fig. 1(c) for the $I_{BP}$ distribution], 1304 (80%) of which are randomly picked for training.

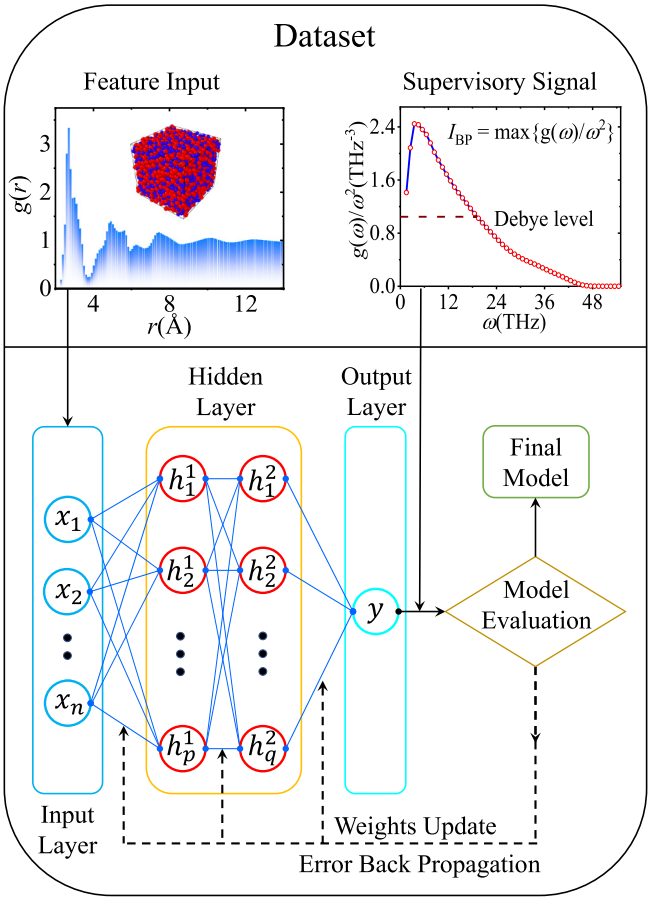


FIG. 2. The architecture and training procedure of a 4-layer neural network model $n - p - q - 1$ which contains two hidden layers with $p$ and $q$ neurons, respectively. The model takes discrete pair distribution function (PDF) as feature inputs, with the boson peak intensity as the final output (supervisory signal).

In terms of the single-particle intensity of the boson peak, the VDOS contributed by each atom is first calculated according to the relative amplitude of a certain vibrational mode:

$$g_i(\omega) = \frac{1}{3N}\sum_{j=1}^{N}\delta(\omega-\omega_j)\left|\mathbf{e}_j^i\right|^2, \tag{4}$$

where $\mathbf{e}_j^i$ represents the eigenvector of atom $i$ corresponding to the intrinsic frequency $\omega_j$. Subsequently, the boson peak contribution of atom $i$ is defined as the maximum of its $\omega^2$-reduced particle VDOS, like that of the whole system, i.e., $I_{BP}^i = \max[g_i(\omega)/\omega^2]$.

### D. Neural network model

The artificial neural network (ANN) is a mathematical computing system which simulates the working mechanism of the biological neurons that constitute human brains. Here, we adopt ANN in dealing with the seemingly unsolved issue in directly connecting atom positions to vibrational properties without turning to detailed atomic interaction.

Figure 2 illustrates the workflow of model learning with the architecture of a four-layer neural network $n - p - q - 1$ included. The leftmost layer, known as the input layer, contains $n$ neurons $\mathbf{x} = \{x_1, x_2, \ldots, x_n\}^\top$, representing the feature inputs. For a training process, neurons in each hidden layer receive the information transmitted from the previous layer with weighted linear summation $h^{in} = \sum_{j=1}^{n_{pre}} w_{pre}^j h_{pre}^{out}$ and pass this information to the next layer after processing them $h^{out} = f(h^{in})$. Connection weights refer to the weighting coefficients between neurons, and the way these neurons process the weighted summation $f : h^{in} \to h^{out}$ is called the activation

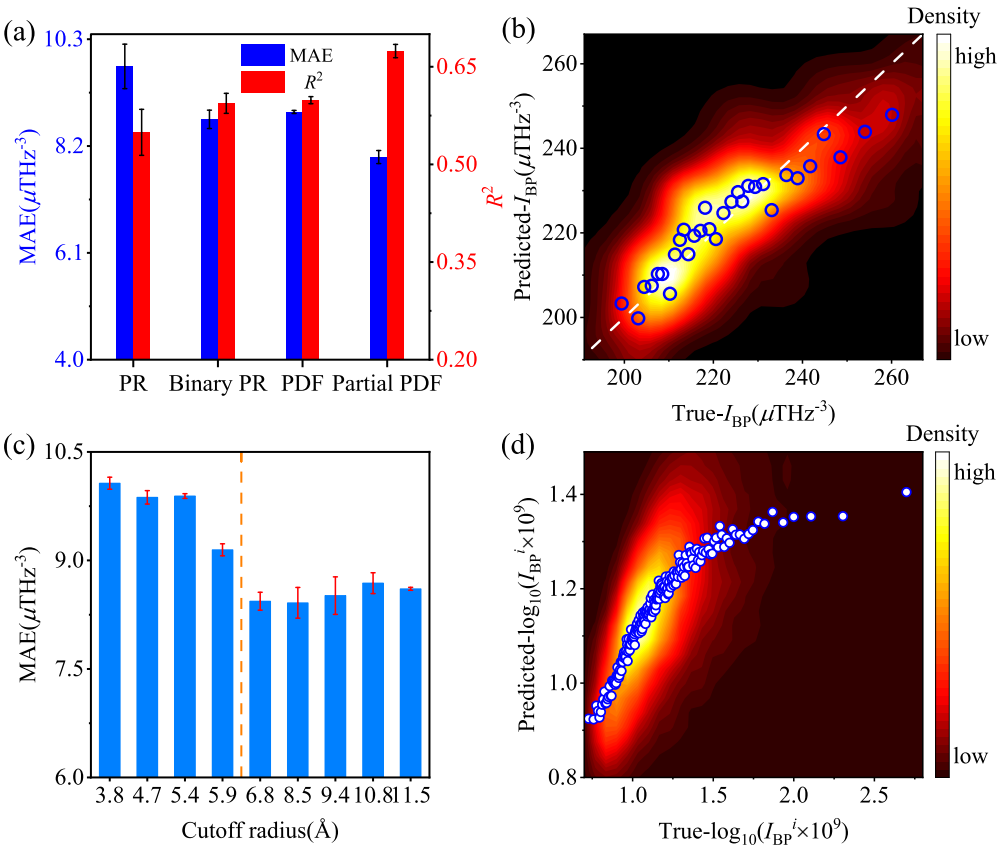


FIG. 3. Predictive performance of the artificial neural network (ANN) model. (a) Mean absolute error (MAE) and $R^2$ score of four different feature inputs: participation ratio (PR), binary PR, total pair distribution function (PDF), and partial PDF. (b) The predicted intensity of boson peak as a function of the true $I_{BP}$ value in the testing dataset at sample level. The white dashed line represents a perfect prediction: $I_{BP\text{-}pre} = I_{BP\text{-}true}$, while the scattered blue circles represent numerically coarse-grained values with bin size of 10 samples. (c) The testing MAE of $I_{BP}$ as a function of the cutoff radius. (d) The predicted intensity of atomic-scale boson peak as a function of the true $I^i_{BP}$ value in the testing dataset.

function. Neurons in the output layer also have activation functions that transform the received values into the final outputs. Based on the error between the predicted and actual values, the connection weights are updated by the error back propagation algorithm to adjust predictions. Such a loop continues until the model tends toward convergence.

Except the quality of the dataset, the predictive performance of the neural network model is also affected by many factors termed hyperparameters, such as learning rate, the number of layers, the number of neurons in each layer, and the optimizer. Before formal learning, we tested a series of parameter combinations to approach the best prediction as far as possible and finally selected Adadelta as the optimizer [55]. The original learning rate is set to 0.01, and methods including early stopping, dropout and regularization are adopted to avoid overfitting. The training and testing processes are implemented by the Keras API on top of the TensorFlow backend [56].

## III. RESULTS AND DISCUSSION

As introduced in the Methods section, we try to quantify the origin of the boson peak in glass both dynamically and structurally by means of the ANN model, with different feature inputs employed: participation ratio, binarized participation ratio, total PDF, and partial PDF, respectively. Particulars of these models are described in Appendix B, and their predictive powers are plotted in Fig. 3(a). Note that all four cases share the same training and testing set to fairly compare their expressive power. Interestingly, the binarized participation ratio which outlines the degree of vibrational localization yields results like that of the total PDF, emphasizing the connection between the boson peak and the quasilocalized modes. The ML model prediction agrees with the physical understanding from direct normal mode analysis by Wang *et al.* [53]. The partial PDF manifests the best results of the four kinds of feature input and obviously outperforms the total PDF in MAE by 12.6% (7.98 vs 9.13 $\mu$THz$^{-3}$), indicating that the boson peak is relevant to specific distributions of component atoms and their interactions [57]. The predictive performance of the partial PDF is illustrated in Fig. 3(b), where the background shows the raw data colored by number density, and the scattered blue circles represent numerically coarse-grained values with bin size of 100 atoms. All the data points roughly lie along an ideal prediction: $I_{BP\text{-}pre} = I_{BP\text{-}true}$ except for some deviation at high $I_{BP}$. The MAE is equivalent to 7.98 $\mu$THz$^{-3}$, which accounts for 8.67% of the

whole $I_{\text{BP-true}}$ span (maximum: 285.30 $\mu\text{THz}^{-3}$, minimum: 193.21 $\mu\text{THz}^{-3}$) of the testing set.

To go a step further, the partial PDFs with different cutoff radii are utilized as feature inputs to train the ANN model. Figure 3(c) illustrates the corresponding MAE. Because the optimization may converge to a local minimum, the training and testing procedure is repeated 9 times for each case (red error bars). Note that all these results are obtained by the ML models trained on the same dataset and under the same hyperparameter setting without optimization, so they indeed portray the influence of cutoff radii on the predictive performance, though they are not the best for each case. With the increase of cutoff radius, MAE gradually decreases and tends to stabilize when it reaches 6.85 Å. For the partial PDFs of Cu-Cu and Cu-Zr, the length scale of 6.85 Å corresponds to the fourth coordination shell, while for the partial PDF of Zr-Zr, it is the third one. This implies a nonlocal attribute of the boson peak with a characteristic subnanometer length scale that needs to be considered when deciphering its structural origin, as uncovered in many other structure-property relationships of amorphous solids [12,35,40,58–61]. Note that predictions of the glasses with the highest 12.31% $I_{\text{BP}} > 249.34\,\mu\text{THz}^{-3}$ exhibit more deviation from true values than average. For one thing, the dataset here contains only 1629 configurations in total, resulting in a lack of data points with, in particular, high $I_{\text{BP}}$. Furthermore, the one-dimensional PDF providing only statistical structural information cannot portray accurately how the atoms are arranged in the three-dimensional (3D) space. The two reasons stated above result in perfect predictions being impossible and therefore point out directions toward accurate quantification of the boson peak from 3D complete structures in glass.

To evaluate whether the ANN model is applicable to different atoms in quantifying the boson peak, we also test the ML model at atomic level following the same procedure as detailed above except for some differences in the supervisory signal and the feature input. Here, the feature input of specific atoms contains four channels: Cu-Cu, Cu-Zr, Zr-Cu, and Zr-Zr, respectively. For Cu atoms, Zr-centered channels are correspondingly set to zero and vice versa. The extension of the ANN model to atoms is displayed in Fig. 3(d). Though the atomic-scale predictive performance is inferior to that of the whole sample, the predicted $I_{\text{BP}}^i$ and the true values correlate positively and exhibit considerable linearity when $I_{\text{BP}}^i$ is $<0.00186\,\mu\text{THz}^{-3}$ (accounting for 89.10% of the testing set). Similarly, in Appendix C, the atomic partial PDF exhibits a characteristic length scale close to that of the samples, indicating that the boson peak shares the same structural origin regardless of length scales of glasses.

For atoms with the highest and lowest 10% $I_{\text{BP}}^i$, both the predicted and real values, we plot all four partial PDFs. Figure 4 illustrates the differences to unveil the key structural fingerprints underneath the boson peak. It is observed that atoms with higher peaks and shallower basins tend to display lower boson peak intensity. For atoms with the highest 10% $I_{\text{BP}}^i$, the first peak of their PDF shifts closer to the central atom, while the second peak moves farther, resulting in a wider trough between them. This wider trough with generally larger intensity than that of the other group, along with those lower peaks, demonstrates a more liquidlike, disordered structure with more mobility. These differences are obvious for the first three or four neighbor shells and soon wear off beyond some scale, explaining the predictive performance trend in Fig. 3(c). Additionally, the highest $I_{\text{BP}}^i$ group exhibits a larger first peak intensity ratio of the two PDF channels, $g(r)_{\alpha\text{-}\beta}/g(r)_{\alpha\text{-}\alpha}$ ($\alpha$ can be either Cu or Zr and $\beta$ is the other element). Such a larger deviation from the system component ratio (50 : 50) implies the influence of chemical disorder on the boson peak. Except that the partial PDFs of Zr atoms with extremely low $I_{\text{BP}}^i$ display some quantitative errors, all the other ones exhibit a good overlap between the solid lines (real) and the scattered data points (predicted), revealing the power of the ANN model in qualitatively predicting boson peak intensity based on structural information.

Although the ML model usually indicates a numerical solution with sort of black-box information, the present protocol allows one to interpret it since the learning feature is the PDF which can recognize key short- to medium-range structural morphology. As shown in Fig. 5(a), the overall difference in the total PDF of these samples is so trivial that it is difficult to quantify the $I_{\text{BP}}$ based on the PDF with a simple function mapping, while ANN makes a difference. To illustrate the mapping ability of the ANN model, we compress the hidden layer block into a single neuron for simplicity without detracting from representativeness. As illustrated in Fig. 5(b), the 120 trained connection weights between the first input layer and the hidden neuron are extracted, which correlate well with the PDF difference, taking negative or positive values as the difference undulates. Note that, for partial PDFs, these weights of different channels interact in a complex manner and may not be fully consistent with the partial PDF difference. Through the training process, the hidden neurons adjust them recurrently to recognize the seemingly negligible difference in the PDF until approaching the final output. The excellent mapping capability of ANN just lies in the combination of such neurons together with the activation functions which introduce nonlinearity into the model. In other words, the ANN model recognizes subtle structural features of the boson peak which points to a scenario of short- to medium-range disorder-induced phonon damping in glass.

The reasons why ANN fails at predicting the data points with high $I_{\text{BP}}^i$ possibly include (1) heavy-tailed distribution of $I_{\text{BP}}^i$ that spans four orders of magnitude (minimum: 0.004657 $\mu\text{THz}^{-3}$, maximum: 2.8310 $\mu\text{THz}^{-3}$), which results in less statistically meaningful data for the high-$I_{\text{BP}}^i$ regime. The data imbalance issue may be solved further by enlarging the dataset or through standardization of the raw data. (2) As a structural descriptor, the particle-level partial PDF is inadequate. More detailed 3D coordinate information is required in the learning process. (3) There is no one-to-one causal relationship between atomic-scale structure and function of disordered materials [61,62]. Statistical information of local structures is more relevant for the boson peak. (4) The boson peak has a collective nature, which should include a group of neighboring atoms that can constitute some vibrational pattern like the acoustic transverse localized model [9]. Such

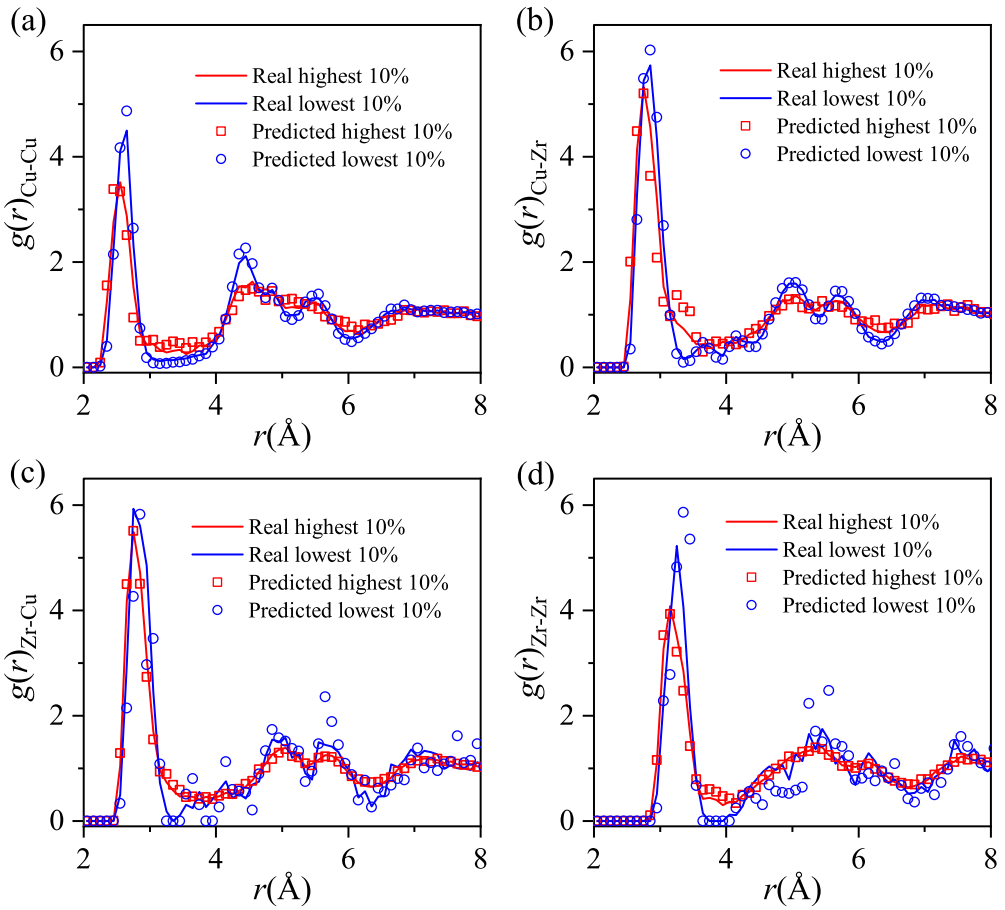


FIG. 4. Four partial pair distribution functions (PDFs) of two groups of atoms with the highest and lowest 10% atomic boson peak intensity $I^i_{\text{BP}}$. Solid lines represent the real $I^i_{\text{BP}}$, while scattered points represent the predicted ones.

circumstances again appeal for more representative datasets and better descriptors.

## IV. CONCLUSIONS

In summary, we present a preliminary attempt to quantify the boson peak by virtue of possible local structure and from the perspective of vibrational localization in a $Cu_{50}Zr_{50}$ binary glass-forming system through a ML strategy. The binary participation ratio can yield results comparable with that of the total PDF, implying the connection between quasilocalized modes and the boson peak phenomenon. The partial PDF provides the best predictive performance of all four kinds of feature inputs, a prediction with MAE equal to 7.98 $\mu\text{THz}^{-3}$. The model recognizes several subtle structural features in the first several neighbor shells of the partial PDF responsible for the boson peak. By adjusting the cutoff radius of the partial PDF as the feature input, we demonstrate that there exists a subnanometer length scale that is strongly associated with the boson peak, at both sample and atomic level regardless of the size of glasses. This length scale characterizes the elastic heterogeneity of glass and indicates the spatial nature of the Ioffe-Regal limit. The phonons become damped at such a scale due to the appearance of structural patterns that hinders the propagation of an elastic wave. Since the current predictive

TABLE I. Specific architecture of the ANN models utilized.

| | | Architecture | | |
|---|---|---|---|---|
| Level | Feature input | 1 | 2 | 3 |
| Sample | PR | 724-200-100-1 | 724-100-50-1 | 724-100-1 |
| | Binary PR | 724-200-100-1 | 724-100-50-1 | 724-100-1 |
| | PDF | 120-60-30-1 | 120-60-1 | 120-30-1 |
| | Partial PDF | 360-100-50-1 | 360-50-1 | 360-20-1 |
| Atom | Partial PDF | 480-100-50-1 | 480-50-1 | 480-20-1 |

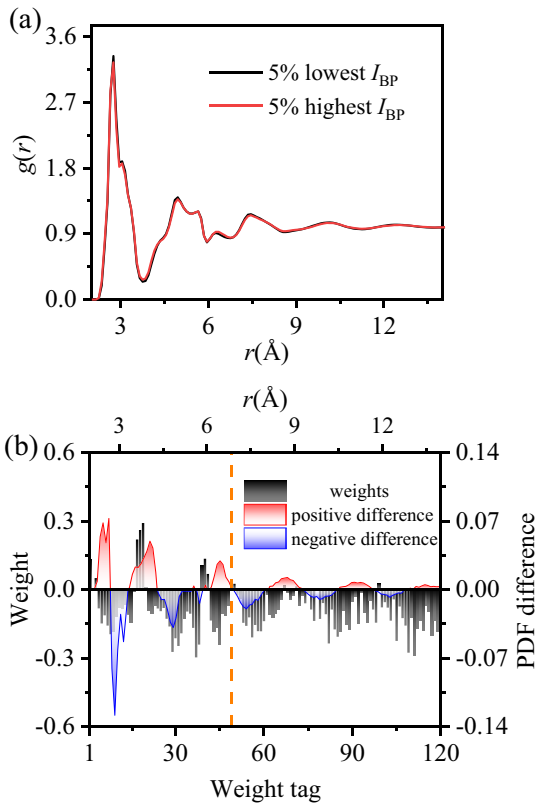


FIG. 5. Correlation between total pair distribution function (PDF) and the learned weights of the neural network model. (a) PDFs of the $Cu_{50}Zr_{50}$ metallic glass samples with the 5% lowest and the 5% highest intensity of boson peak. (b) Connection weights between the input layer and the first hidden layer compared with the PDF difference $[g^{high}(r) - g^{low}(r)]$ of the two classes of glass samples with extreme boson peak intensity mentioned in (a).

performance is obtained solely with PDFs, a one-dimensional statistical structure descriptor, and a relatively small dataset consisting of 1629 configurations, we believe that there is still much room for improvement when a larger dataset is deployed and more delicate structural descriptors are utilized. Thus, in this paper, we shed light on accurate prediction of the boson peak from pure structural information. Although the predictive power of the ML model is still not fully satisfactory, it presents a first step toward understanding the structural motif responsible for this vibrational anomaly in amorphous solids, which is a longstanding unsolved problem in condensed matter physics.

## ACKNOWLEDGMENTS

This paper was financially supported by National Natural Science Foundation of China (Grant No. 12072344) and the Youth Innovation Promotion Association of the Chinese Academy of Sciences. The numerical calculations in this paper were carried out on the ORISE Supercomputer.

## APPENDIX A: PARTICIPATION RATIO AND THRESHOLD

As shown in Fig. 6, the participation ratio $P(\omega)$ measures the degree of localization of a specific vibrational mode. The

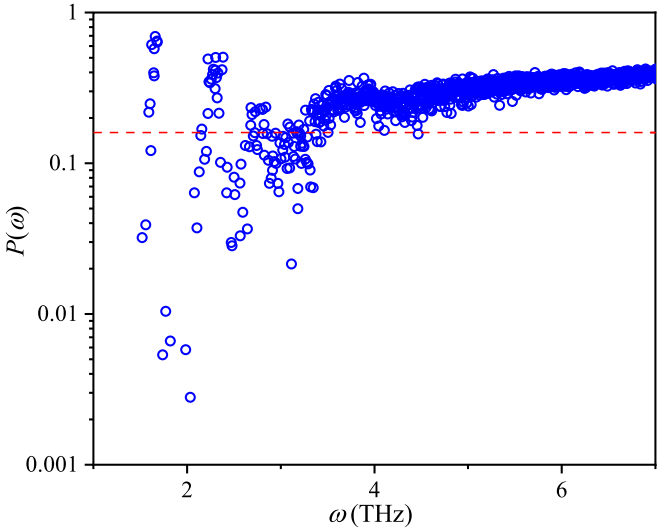


FIG. 6. Participation ratio $P(\omega)$ as a function of intrinsic frequency $\omega$ in a glass sample with 19 652 atoms. Red dashed line represents the threshold $P_0$ used to classify vibrational modes into extended and quasilocalized categories.

more $P(\omega)$ approaches 1, the more equally all the atoms participate in the vibrational mode. In turn, the more $P(\omega)$ approaches $N^{-1}$, the fewer atoms get involved in the vibration. The choice of the threshold $P_0$ (cutoff criterion for dividing modes into extended or quasilocalized groups) is therefore crucial to the final performance of ANN model when we use the binary $P(\omega)$ as a feature input to quantify the boson peak intensity. Here, to avoid arbitrariness, we have tested different thresholds between 0.02 and 0.40 with intervals of 0.02. Naturally, all the models behave the best when $P_0$ ranges from 0.24 to 0.30 as shown in Fig. 7. This trend emphasizes the intrinsic connection between the low-frequency quasilocalized modes

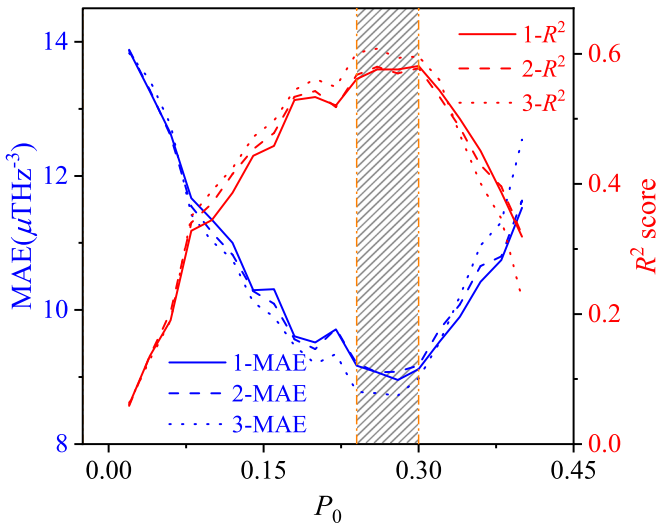


FIG. 7. For the binary participation ratio (PR) as feature input, mean absolute error (MAE) and $R^2$ score as a function of the threshold $P_0$. The results here are obtained similarly in Appendix B. The solid, dashed, and dotted lines represent the architectures 1, 2, and 3 in Table I, respectively.

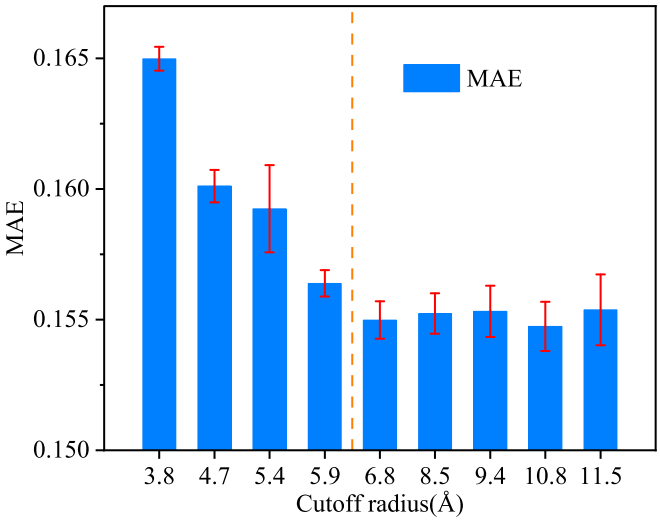


FIG. 8. The testing mean absolute error of $\log_{10}(I^i_{\rm BP} \times 10^9)$ as a function of the cutoff radius of the partial pair distribution functions (PDFs). For each cutoff radius, the training and testing procedure is repeated 9 times.

and the boson peak phenomenon. We finally choose $P_0 = 0.28$ as the threshold of the binary $P(\omega)$.

## APPENDIX B: PARTICULARS OF DIFFERENT ANN MODELS

For each feature input, we have tried three ANN architectures (in Table I) with different numbers of hidden layers and hidden neurons to obtain a better representative result, though there are only small differences. We also repeat the training and testing procedure 9 times for each architecture to eliminate contingency. The best average results of the three architectures are selected and illustrated in Fig. 3(a).

## APPENDIX C: ABOUT THE LENGTH SCALE AT ATOMIC LEVEL

Following the practice in Fig. 3(c), we test the influence of the cutoff radius on the model performance when using the partial PDF to regress $I^i_{\rm BP}$. As illustrated in Fig. 8, we get similar results to that of the samples. Both stabilize at the same length scale of 6.85 Å.


[1] R. C. Zeller and R. O. Pohl, Thermal conductivity and specific heat of noncrystalline solids, Phys. Rev. B **4**, 2029 (1971).
[2] M. P. Zaitlin and A. C. Anderson, Phonon thermal transport in noncrystalline materials, Phys. Rev. B **12**, 4475 (1975).
[3] J. J. Freeman and A. C. Anderson, Thermal conductivity of amorphous solids, Phys. Rev. B **34**, 5684 (1986).
[4] V. K. Malinovsky, V. N. Novikov, P. P. Parshin, A. P. Sokolov, and M. G. Zemlyanov, Universal form of the low-energy (2 to 10 meV) vibrational spectrum of glasses, Europhys. Lett. **11**, 43 (1990).
[5] Y. Yu, C. Yang, M. Baggioli, A. E. Phillips, A. Zaccone, L. Zhang, R. Kajimoto, M. Nakamura, D. Yu, and L. Hong, The $\omega^3$ scaling of the vibrational density of states in quasi-2D nanoconfined solids, Nat. Commun. **13**, 3649 (2022).
[6] S. Ren, H.-X. Zong, X.-F. Tao, Y.-H. Sun, B.-A. Sun, D.-Z. Xue, X.-D. Ding, and W.-H. Wang, Boson-peak-like anomaly caused by transverse phonon softening in strain glass, Nat. Commun. **12**, 5755 (2021).
[7] T. Nakayama, Boson peak and terahertz frequency dynamics of vitreous silica, Rep. Prog. Phys. **65**, 1195 (2002).
[8] H. Shintani and H. Tanaka, Universal link between the boson peak and transverse phonons in glass, Nat. Mater. **7**, 870 (2008).
[9] Y. C. Hu and H. Tanaka, Origin of the boson peak in amorphous solids, Nat. Phys. **18**, 669 (2022).
[10] U. Buchenau, Y. M. Galperin, V. L. Gurevich, and H. R. Schober, Anharmonic potentials and vibrational localization in glasses, Phys. Rev. B **43**, 5039 (1991).
[11] V. L. Gurevich, D. A. Parshin, and H. R. Schober, Anharmonicity, vibrational instability, and the boson peak in glasses, Phys. Rev. B **67**, 094203 (2003).
[12] Z. Y. Yang, Y. J. Wang, and A. Zaccone, Correlation between vibrational anomalies and emergent anharmonicity of the local potential energy landscape in metallic glasses, Phys. Rev. B **105**, 014204 (2022).
[13] S. R. Elliott, A unified model for the low-energy vibrational behaviour of amorphous solids, Europhys. Lett. **19**, 201 (1992).
[14] W. Schirmacher, Thermal conductivity of glassy materials and the "boson peak", Europhys. Lett. **73**, 892 (2006).
[15] F. Léonforte, A. Tanguy, J. P. Wittmer, and J.-L. Barrat, Inhomogeneous Elastic Response of Silica Glass, Phys. Rev. Lett. **97**, 055501 (2006).
[16] W. Schirmacher, G. Ruocco, and T. Scopigno, Acoustic Attenuation in Glasses and its Relation with the Boson Peak, Phys. Rev. Lett. **98**, 025501 (2007).
[17] A. Marruzzo, W. Schirmacher, A. Fratalocchi, and G. Ruocco, Heterogeneous shear elasticity of glasses: the origin of the boson peak, Sci. Rep. **3**, 1407 (2013).
[18] S. Gelin, H. Tanaka, and A. Lemaître, Anomalous phonon scattering and elastic correlations in amorphous solids, Nat. Mater. **15**, 1177 (2016).
[19] A. Zaccone and E. Scossa-Romano, Approximate analytical description of the nonaffine response of amorphous solids, Phys. Rev. B **83**, 184205 (2011).
[20] R. Milkus and A. Zaccone, Local inversion-symmetry breaking controls the boson peak in glasses and crystals, Phys. Rev. B **93**, 094204 (2016).
[21] T. S. Grigera, V. Martín-Mayor, G. Parisi, and P. Verrocchio, Phonon interpretation of the "boson peak" in supercooled liquids, Nature (London) **422**, 289 (2003).
[22] J. Yang, Y. J. Wang, E. Ma, A. Zaccone, L. H. Dai, and M. Q. Jiang, Structural Parameter of Orientational Order to Predict the Boson Vibrational Anomaly in Glasses, Phys. Rev. Lett. **122**, 015501 (2019).
[23] S. N. Taraskin, Y. L. Loh, G. Natarajan, and S. R. Elliott, Origin of the Boson Peak in Systems with Lattice Disorder, Phys. Rev. Lett. **86**, 1255 (2001).
[24] A. I. Chumakov, G. Monaco, A. Monaco, W. A. Crichton, A. Bosak, R. Rüffer, A. Meyer, F. Kargl, L. Comez, D. Fioretto

*et al.*, Equivalence of the Boson Peak in Glasses to the Transverse Acoustic van Hove Singularity in Crystals, Phys. Rev. Lett. **106**, 225501 (2011).

[25] W. Schirmacher, G. Diezemann, and C. Ganter, Harmonic Vibrational Excitations in Disordered Solids and the "Boson Peak", Phys. Rev. Lett. **81**, 136 (1998).

[26] A. Agrawal and A. Choudhary, Perspective: Materials informatics and big data: Realization of the "fourth paradigm" of science in materials science, APL Mater. **4**, 053208 (2016).

[27] Y. Mishin, Machine-learning interatomic potentials for materials science, Acta Mater. **214**, 116980 (2021).

[28] T. Wen, L. Zhang, H. Wang, W. E, and D. J. Srolovitz, Deep potentials for materials science, Mater. Futures **1**, 022601 (2022).

[29] H. Liu, Z. Fu, K. Yang, X. Xu, and M. Bauchy, Machine learning for glass science and engineering: A review, J. Non-Cryst. Solids **557**, 119419 (2021).

[30] J. Behler and M. Parrinello, Generalized Neural-Network Representation of High-Dimensional Potential-Energy Surfaces, Phys. Rev. Lett. **98**, 146401 (2007).

[31] F. Ren, L. Ward, T. Williams, K. J. Laws, C. Wolverton, J. Hattrick-Simpers, and A. Mehta, Accelerated discovery of metallic glasses through iteration of machine learning and high-throughput experiments, Sci. Adv. **4**, eaaq1566 (2018).

[32] Q. Wang and L. Zhang, Inverse design of glass structure with deep graph neural networks, Nat. Commun. **12**, 5359 (2021).

[33] E. D. Cubuk, S. S. Schoenholz, J. M. Rieser, B. D. Malone, J. Rottler, D. J. Durian, E. Kaxiras, and A. J. Liu, Identifying Structural Flow Defects in Disordered Solids Using Machine-Learning Methods, Phys. Rev. Lett. **114**, 108001 (2015).

[34] S. S. Schoenholz, E. D. Cubuk, D. M. Sussman, E. Kaxiras, and A. J. Liu, A structural approach to relaxation in glassy liquids, Nat. Phys. **12**, 469 (2016).

[35] E. D. Cubuk, R. J. S. Ivancic, S. S. Schoenholz, D. J. Strickland, A. Basu, Z. S. Davidson, J. Fontaine, J. L. Hor, Y.-R. Huang, Y. Jiang *et al.*, Structure-property relationships from universal signatures of plasticity in disordered solids, Science **358**, 1033 (2017).

[36] Q. Wang and A. Jain, A transferable machine-learning framework linking interstice distribution and plastic heterogeneity in metallic glasses, Nat. Commun. **10**, 5537 (2019).

[37] V. Bapst, T. Keck, A. Grabska-Barwińska, C. Donner, E. D. Cubuk, S. S. Schoenholz, A. Obika, A. W. R. Nelson, T. Back, D. Hassabis *et al.*, Unveiling the predictive power of static structure in glassy systems, Nat. Phys. **16**, 448 (2020).

[38] Z. Fan, J. Ding, and E. Ma, Machine learning bridges local static structure with multiple properties in metallic glasses, Mater. Today **40**, 48 (2020).

[39] Z. Fan and E. Ma, Predicting orientation-dependent plastic susceptibility from static structure in amorphous solids via deep learning, Nat. Commun. **12**, 1506 (2021).

[40] Z. Y. Yang, D. Wei, A. Zaccone, and Y. J. Wang, Machine-learning integrated glassy defect from an intricate configurational-thermodynamic-dynamic space, Phys. Rev. B **104**, 064108 (2021).

[41] Z. H. Peng, Z. Y. Yang, and Y. J. Wang, Machine learning atomic-scale stiffness in metallic glass, Extreme Mech. Lett. **48**, 101446 (2021).

[42] A. P. Thompson, H. M. Aktulga, R. Berger, D. S. Bolintineanu, W. M. Brown, P. S. Crozier, P. J. in 't Veld, A. Kohlmeyer, S. G. Moore, T. D. Nguyen *et al.*, LAMMPS—A flexible simulation tool for particle-based materials modeling at the atomic, meso, and continuum scales, Comput. Phys. Commun. **271**, 108171 (2022).

[43] M. I. Mendelev, Y. Sun, F. Zhang, C. Z. Wang, and K. M. Ho, Development of a semi-empirical potential suitable for molecular dynamics simulation of vitrification in Cu-Zr alloys, J. Chem. Phys. **151**, 214502 (2019).

[44] S. Nosé, A molecular dynamics method for simulations in the canonical ensemble, Mol. Phys. **52**, 255 (1984).

[45] W. G. Hoover, Canonical dynamics: Equilibrium phase-space distributions, Phys. Rev. A **31**, 1695 (1985).

[46] M. Parrinello and A. Rahman, Polymorphic transitions in single crystals: A new molecular dynamics method, J. Appl. Phys. **52**, 7182 (1981).

[47] P. M. Piaggi, O. Valsson, and M. Parrinello, Enhancing Entropy and Enthalpy Fluctuations to Drive Crystallization in Atomistic Simulations, Phys. Rev. Lett. **119**, 015701 (2017).

[48] E. Lerner, G. Düring, and E. Bouchbinder, Statistics and Properties of Low-Frequency Vibrational Modes in Structural Glasses, Phys. Rev. Lett. **117**, 035501 (2016).

[49] H. Mizuno, H. Shiba, and A. Ikeda, Continuum limit of the vibrational properties of amorphous solids, Proc. Natl. Acad. Sci. USA **114**, E9767 (2017).

[50] G. Kapteijns, E. Bouchbinder, and E. Lerner, Universal Nonphononic Density of States in 2D, 3D, and 4D Glasses, Phys. Rev. Lett. **121**, 055501 (2018).

[51] L. Angelani, M. Paoluzzi, G. Parisi, and G. Ruocco, Probing the non-Debye low-frequency excitations in glasses through random pinning, Proc. Natl. Acad. Sci. USA **115**, 8700 (2018).

[52] M. Shimada, H. Mizuno, and A. Ikeda, Anomalous vibrational properties in the continuum limit of glasses, Phys. Rev. E **97**, 022609 (2018).

[53] L. Wang, A. Ninarello, P. Guan, L. Berthier, G. Szamel, and E. Flenner, Low-frequency vibrational modes of stable glasses, Nat. Commun. **10**, 26 (2019).

[54] E. Lerner and E. Bouchbinder, Frustration-induced internal stresses are responsible for quasilocalized modes in structural glasses, Phys. Rev. E **97**, 032140 (2018).

[55] M. D. Zeiler, Adadelta: An adaptive learning rate method, arXiv:1212.5701.

[56] M. Abadi, P. Barham, J. Chen, Z. Chen, A. Davis, J. Dean, M. Devin, S. Ghemawat, G. Irving, M. Isard *et al.*, TensorFlow: A system for large-scale machine learning, in *Proceedings of the 12th USENIX Conference on Operating Systems Design and Implementation*, OSDI'16 (USENIX Association, USA, 2016), pp. 265–283.

[57] T. Bryk and I. Mryglod, Concentration fluctuations and boson peak in a binary metallic glass: A generalized collective modes study, Phys. Rev. B **82**, 174205 (2010).

[58] J. Ding, Y. Q. Cheng, and E. Ma, Charge-transfer-enhanced prism-type local order in amorphous $Mg_{65}Cu_{25}Y_{10}$: Short-to-medium-range structural evolution underlying liquid fragility and heat capacity, Acta Mater. **61**, 3130 (2013).

[59] H. Tong and H. Tanaka, Revealing Hidden Structural Order Controlling Both Fast and Slow Glassy Dynamics in Supercooled Liquids, Phys. Rev. X **8**, 011041 (2018).

[60] Y.-C. Hu, Y.-W. Li, Y. Yang, P.-F. Guan, H.-Y. Bai, and W.-H. Wang, Configuration correlation governs slow dynamics of supercooled metallic liquids, Proc. Natl. Acad. Sci. USA **115**, 6375 (2018).

[61] D. Wei, J. Yang, M. Q. Jiang, B. C. Wei, Y. J. Wang, and L. H. Dai, Revisiting the structure–property relationship of metallic glasses: Common spatial correlation revealed as a hidden rule, Phys. Rev. B **99**, 014115 (2019).

[62] D. Wei, J. Yang, M.-Q. Jiang, L.-H. Dai, Y.-J. Wang, J. C. Dyre, I. Douglass, and P. Harrowell, Assessing the utility of structure in amorphous materials, J. Chem. Phys. **150**, 114502 (2019).